

pubs.acs.org/cm Article

Large Mid-Infrared Second-Harmonic Generation in Eu(II)-Based Quaternary Chalcogenides

Published as part of Chemistry of Materials special issue "In Memory of Prof. Francis DiSalvo".

Subhendu Jana, Eric A. Gabilondo, Machima Mongkhonratanachai, Yujie Zhang, P. Shiv Halasyamani, and Paul A. Maggard*



Cite This: Chem. Mater. 2024, 36, 9750-9761



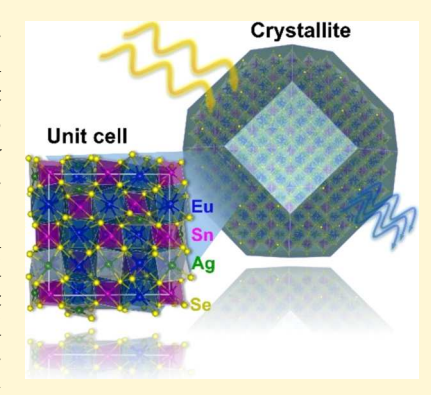
ACCESS

III Metrics & More

Article Recommendations

s Supporting Information

ABSTRACT: Complex metal chalcogenides have received growing attention for second-harmonic generation (SHG) activity arising from their noncentrosymmetric structures. In this area, the impact of the Eu(II)-cation on their structures and optical properties has not been well explored. Synthetic investigations of the Eu–Ag–IV-Ch (IV = Sn or Ge; Ch = S or Se) systems have unveiled four Eu(II)-based quaternary chalcogenides exhibiting very large mid-IR SHG responses within the chemically rich systems II–I₂-IV-Ch₄ and II₃–I₂-IV₂–Ch₈ (Ch = S or Se; I, II, and IV = monovalent, divalent, and tetravalent cations, respectively). Their structures were characterized by single-crystal X-ray diffraction methods to crystallize in noncentrosymmetric space groups, I42m for EuAg₂GeS₄ (1) and I43d for Eu₃Ag₂Ge₂Se₈ (2) Eu₃Ag₂Sn₂Se₈ (3), and Eu₃Ag₂Sn₂Sg (4). The structures consist of body-centered arrangements of (Ge/Sn)Ch₄ tetrahedra that are fully oriented and bridged by flattened AgCh₄ tetrahedra into three-dimensional (3D) networks and charge-balanced by Eu(II) cations. Their crystalline powders exhibit mid-IR (2.09 μ m) SHG



responses among the largest reported to date, ranging from $\sim 1.9 \times AGS$ (AgGaS₂) for 1, to increasing activities of ~ 1.9 for 3, ~ 4.7 for 2, and ~ 7.0 for 4 × AGS. Spin-polarized band structure calculations showed that the valence and conduction band edge states stem from interactions of the Ag-to-S/Se-based and Ge/Sn-to-S/Se-based states, respectively, with increasing contributions of the Eu(II) $4f^7$ -based states in the order of 1 < 3 < 2 < 4. Interestingly, this trend correlates with the SHG activity, suggesting a potential new relationship for understanding and attaining cutting-edge SHG properties within Eu(II)-based chalcogenides. Thus, this family helps tounveil a deeper understanding of structure—optoelectronic/SHG property relationships.

1. INTRODUCTION

Multinary metal chalcogenides have represented some of the most promising compounds for their advanced nonlinear optical (NLO) properties stemming from noncentrosymmetric crystal structures. Materials with NLO properties have wide potential applications, for example, in healthcare, remote sensing,² CO₂ detection,³ and military security.⁴ Within this area, metal chalcogenides have demonstrated among the largest second-harmonic generation (SHG) responses and laser-induced damage threshold (LIDT) for infrared NLO applications, with AgGaCh₂ (Ch = S and Se) and ZnGeP₂ serving as benchmark compounds.⁵ However, the AgGaCh₂ compounds exhibit poor LIDT and ZnGeP2 shows nonnegligible optical absorption in the wavelength range of 0.7-2 μ m. A related compound, γ -NaAsSe₂, shows one of the highest known SHG responses (\sim 75 × AgGaS₂),^{6,7} but is unstable in an ambient atmosphere and undergoes a phase transition to a centrosymmetric polymorph. Prominent challenges for an ideal NLO material include exhibiting a maximal possible SHG response while remaining stable in air, as well as possessing a

high LIDT and a wide transparency window as compared to commercial ${\rm AgGaS_2}^{.8-10}$

Synthesis of multinary metal chalcogenides has remained an active and longstanding area of research for solid-state scientists because of their rich structural chemistry and the wide variation and tunability of their physical properties. 11–16 Thus, a prominent strategy for attaining advanced NLO properties has been to synthetically target chemical substitutions within noncentrosymmetric structure types, such as those for the chalcopyrite and related diamond-type structures. For example, the incorporation of rare-earth elements into chalcophosphates has been demonstrated to significantly improve the LIDT without sacrificing the SHG response magnitude. 17,18 Additionally, co-substitution of alkali or

Received: July 7, 2024
Revised: September 6, 2024
Accepted: September 9, 2024
Published: September 19, 2024





alkaline earth metals with main-group metal cations such as Sn(IV) and Ge(IV) has been found to increase their band gaps and inhibit multiphoton absorptions by removing d-d or f-f transitions. 19 Effective leveraging of these combined strategies was pursued herein in the synthetic exploration of air-stable noncentrosymmetric chalcogenides within the chemically rich II-I-IV-Ch (II = Ba, Sr, Pb, or Eu; I = Li, Cu, or Ag; IV = Si, Ge, or Sn; Ch = S or Se) systems. Prior studies have revealed that compounds in these systems commonly occur with the II-I2-IV-Ch4 and II3-I2-IV2-Ch8 compositions and with noncentrosymmetric, SHG-active, structures. Known examples in the II-I2-IV-Ch4 system form in one of the seven noncentrosymmetric space groups: $\overline{I42}m$ (II = Ba, Sr, or Eu, I = Li or Ag, IV = Si, Ge, or Sn, and Ch = S or Se), 20-25 I222 $(BaAg_2SnS_4)^{23}$, $P3_1$ or $P3_2$ enantiomers (II = Ba or Sr, I = Cu, $IV = Sn \text{ or } Ge, \text{ and } Ch = S),^{26-28} P3_121 \text{ or } P3_221 \text{ enantiomers}$ (II = Ba, Sr, or Eu, I = Cu or Ag, IV = Si, Ge or Sn, and Ch = S or Se), $^{21,26,29-31}$ and Ama2 (II = Eu, I = Cu, IV = Ge or Sn, and X = S or Se). Among these, those formed in the $\overline{14}2m$ space group are related to the chalcopyrite structure type and typically show enhanced SHG activity. Conversely, compounds with the II₃-I₂-IV₂-Ch₈ composition forming in the noncentrosymmetric $I\overline{43}d$ space group include $Sr_3Ag_2Si_2S_8$, $Sr_3Ag_2Sn_2S_8$, $Sr_3Ag_2S_8$, $Sr_3Ag_2S_8$, Ssystems has been relatively well explored, the known Eu(II)based analogues are much more limited. The few known Eu(II)-based chalcogenides in these systems crystallize in alternate structure types, e.g., Li₂EuGeS₄ or Cu₂Eu(Ge,Si)Se₄, and exhibit low or no reported SHG activity. 25,29,3

Described herein is the synthetic preparation of four Eu(II)based quaternary chalcogenides with large mid-IR SHG activities and noncentrosymmetric structures crystallizing in the desired $\overline{142}m$ or $\overline{143}d$ space groups. These compounds were formed during high-temperature synthetic investigations in the $EuAg_2IVCh_4$ and $Eu_3Ag_2IV_2Ch_8$ (IV = Sn or Ge; Ch = S, Se) systems and represent the first reported compounds within the Eu-Ag-IV-Ch quaternary systems. While EuAg₂GeS₄ had been investigated theoretically,³³ it had not been synthesized previously. Each was synthesized as single crystals for structure determination as well as in bulk powder form. Additional characterization methods included temperaturedependent magnetic susceptibility, ultraviolet-visible (UVvis) diffuse reflectance spectroscopy, and SHG activity at a mid-infrared wavelength of 2.09 μ m. Their electronic structures were also probed with the use of spin-polarized electronic structure calculations, revealing the impact of the atomic contributions and, especially, the Eu(II) 4f7-based states to the band edge states, band gap types, band dispersions, as well as SHG activity.

2. EXPERIMENTAL SECTION

2.1. Reagents Used. Single crystals and bulk polycrystalline powders of 1 to 4 were synthesized using the following reagents: Eu ingot (Alfa Aesar, 99.9% purity), Ag₂S powder (Alfa Aesar, 99.99% purity), Ag powder (Alfa Aesar, 99.99% purity), Sn ingot (Alfa Aesar, 99.99% purity), Ge powder (Alfa Aesar, 99.99% purity), and Se powder (Alfa Aesar, 99.99% purity). As Eu metal is air-sensitive, all of the chemical manipulations were carried out inside an argon-filled dry glovebox.

2.1.1. Synthesis of EuAg₂GeS₄ (1). Transparent yellow-colored single crystals of I were synthesized from stoichiometric starting materials of Ag₂S powder (43.6 mg, 0.176 mmol), Eu metal chunk (26.7 mg, 0.176 mmol), Ge ingot (12.8 mg, 0.176 mmol), and S

powder (16.9 mg, 0.527 mmol), which were loaded into a 6 mm outer diameter (OD) and 4 mm inner diameter (ID) fused silica tube inside the Ar-filled dry glovebox. The reaction ampule was then evacuated to 10⁻⁴ Torr and sealed with a flame torch. This was then heated to 1123 K in 10 h inside a programmable muffle furnace. The furnace was then annealed for 60 h before slowly cooling to room temperature over 30 h. A pure polycrystalline phase of 1 was synthesized by heating the reactants to 1023 K in 10 h and annealing for 60 h before the furnace was allowed to radiatively cool to room temperature. This product was next ground inside the glovebox and compressed to an 8 mm diameter circular disk using a hydraulic press. The disk was flamesealed again inside an ~12 mm OD fused silica tube. The reaction was annealed for 30 h at 1023 K. The product was then homogeneously ground inside the glovebox, and the phase purity was analyzed using a powder X-ray diffraction. Diffraction peaks were observed, corresponding to the formation of a pure polycrystalline phase of 1.

2.1.2. Syntheses of $Eu_3Ag_2Ge_2Se_8$ (2) and $Eu_3Ag_2Sn_2Se_8$ (3). Transparent block-shaped red-colored single crystals of 2 and 3 were synthesized using identical conditions starting from stoichiometric amounts of Eu metal (31.5 mg, 0.207 mmol), Ag (14.9 mg, 0.138 mmol), Ge (10 mg, 0.138 mmol), and Se (43.6 mg, 0.552 mmol) for 2 and Eu metal (29.6 mg, 0.195 mmol), Ag (14 mg, 0.130 mmol), Sn (15.4 mg, 0.130 mmol), and Se (41 mg, 0.519 mmol) for 3. The elemental starting materials were loaded inside the Ar-filled dry glovebox and vacuum-sealed under $\sim 10^{-4}$ Torr pressure. The tubes were heated to 1123 K in 18 h inside a programmable muffle furnace and then slowly cooled to room temperature at a rate of 20 K h⁻¹. The reaction ampules were opened in air and the products were analyzed separately under an optical microscope to reveal the blockshaped red-colored crystals for each. Relatively high-purity bulk powders of 2 and 3 were synthesized using a two-step solid-state synthesis method from the respective stoichiometric amounts of the elemental starting materials with a total mass of 400 mg for each. The reagents were loaded into a 12 mm outer diameter (OD) carboncoated fused silica tube that was flame-sealed, slowly heated to 1123 K over 16 h, and annealed for 60 h. The resulting ingots were ground inside an Ar-filled glovebox and pressed to a circular disk using a hydraulic press. The disks were next annealed for 48 h at 823 K. The resulting products were characterized by powder XRD analyses and found to be pure polycrystalline phases of 2 and 3.

2.1.3. Synthesis of $Eu_3Ag_2Sn_2S_8$ (4). Red-colored single crystals of 4 were synthesized starting from a 100 mg loaded composition using Eu metal (24.7 mg, 0.163 mmol), Ag (35.1 mg, 0.325 mmol), Sn (19.3 mg, 0.163 mmol), and S (20.9 mg, 0.652 mmol). The reactions were prepared and performed similarly to those described above for 1-3. The reaction was slowly heated to 1023 K over 16 h, annealed for 48 h, and then cooled slowly to 573 K over 20 h. The furnace was next allowed to radiatively cool to room temperature. High-purity bulk powder of 4 was prepared using a two-step solid-state synthesis method, like that described above for 1 to 3. Initially, a stoichiometric amount of elemental starting materials of Eu (98.8 mg, 0.652 mmol), Ag (140.4 mg, 1.300 mmol), Sn (77.2 mg, 0.652 mmol), and S (83.6 mg, 2.608 mmol) were massed and loaded into a carbon-coated fused silica tube that was then flame-sealed. The reaction mixture was heated to 1023 K over 16 h, annealed at that temperature for 60 h, and then allowed to radiatively cool to room temperature. After the product powder was pressed into a circular disk, it was then reheated to 823 K for 48 h. The resulting product was checked by powder XRD analysis to be predominantly polycrystalline 4 with the co-formation of a minute amount of a secondary phase as shown in Figure S6.

2.2. Characterization and Property Measurement Techniques. 2.2.1. Structure Determination Using Single-Crystal XRD. The crystal structures were determined from room-temperature (300 K) single-crystal X-ray diffraction (SCXRD) data sets of suitable yellow and red block-shaped crystals of EuAg₂GeS₄ and Eu₃Ag₂IV₂Ch₈ (IV = Ge and Sn and Ch = S and Se) collected using a monochromatized Mo–K α (λ = 0.71073 Å) radiation source on a Bruker D8 venture diffractometer. Suitable EDS-analyzed crystals of EuAg₂GeS₄ (1), Eu₃Ag₂Ge₂Se₈ (2), Eu₃Ag₂Sn₂Se₈ (3), and Eu₃Ag₂Sn₂S₈ (4) were picked separately on a transparent loop

under viscous Paratone-N oil and mounted on the goniometer head to collect the intensity data. The crystal qualities were judged from initial fast scan data sets of 180 frames. The APEX4 software³⁶ was used to determine the unit cell constants for all four different crystals and entire data sets were collected as intensity data. An operating voltage of 50 kV and a working current of 1.4 mA were used for data collection. Exposure time, frame width, and detector-to-crystal distance of 3 s/frame, 0.5°, and 5 cm, respectively, were used for the separate data collection of the crystals. The intensity data were integrated using the APEX4 program,³⁶ and the absorption corrections were carried out using the multiscan method of the SADABS software.³⁷

The XPREP program³⁸ suggested tetragonal or cubic bodycentered (I) cells for the crystals of 1, 2, 3, and 4. XPREP program indicated the noncentrosymmetric I42m and I43d space groups for the EuAg₂GeS₄ and the Eu₃Ag₂IV₂Ch₈ crystals, respectively. The crystal structures were solved in respective space groups using the direct method of the SHELXS program of the SHELX-14 suite of programs.³⁹ The asymmetric unit of the initial solved model of the crystal structure of 1 gave four crystallographically independent atomic sites, which were then assigned to one Eu, one Ag, one Sn, and one S site based on coordination environments and peak heights. The initial structural solutions of 2, 3, and 4 crystals gave six crystallographically independent atomic sites, which were then further assigned to respective atoms based on peak heights and coordination environments. The final solution model provided one Eu, one IV, two Ag, and two Ch sites. Except for the Ag sites, all other atoms are fully occupied. The atomic positions, anisotropic displacement parameters, weight corrections, and extinction parameters were further refined using the least-squares on the F^2 method of the SHELXL program.⁴⁰

The symmetries of the final models were verified using the ADDSYM program of the PLATON software package.⁴¹ The atomic positions were then standardized using the STRUCTURE TIDY program⁴² of PLATON. The Wyckoff positions and site symmetries are provided in the Supporting Information. The crystallographic refinement and metric details are provided in Table 1 and the Supporting Information.

2.2.2. Characterization of Bulk Polycrystalline Powders by Powder XRD and SEM Techniques. All products were ground in air using a mortar and pestle to prepare homogeneous polycrystalline powders. Room-temperature powder XRD data were collected for all

Table 1. Structural Data and Crystallographic Refinement Details for 1 to 4^a

compound	$EuAg_2GeS_4$	$\mathrm{Eu_{3}Ag_{2}Sn_{2}S_{8}}$	$Eu_3Ag_2Sn_2Se_8$	Eu ₃ Ag ₂ Ge ₂ Se ₈
space group	$I\overline{4}2m$	I 4 3d	I 4 3d	I 4 3d
a (Å)	6.8305(3)	14.2876(3)	14.8559(5)	14.5943(3)
c (Å)	7.5722(7)			
V (Å ³)	353.29(5)	2916.61(18)	3278.7(3)	3108.49(19)
Z	2	8	8	8
$\rho \; (\text{g} \cdot \text{cm}^{-3})$	5.344	5.288	6.205	6.184
$\mu \left(\mathrm{mm}^{-1} \right)$	19.49	19.75	34.26	36.88
$R(F)^b$	0.025	0.020	0.021	0.027
$R_{\rm w} (F_{\rm o}^2)^c$	0.065	0.052	0.050	0.066
S	1.12	1.10	1.10	1.09
no. reflections	3676	15553	11132	10645
no. indep. reflections	301	601	685	656
δF (e Å ⁻³)	1.30 and -1.86	0.86 and -1.51	0.65 and -1.41	1.74 and -2.19
flack param.	0.04	0.04	0.95	0.95

 $^a\lambda$ = 0.71073 Å, T = 300(2) K. $^bR(F) = \sum ||F_o| - |F_c|| / \sum |F_o|$ for $F_o^2 > 2\sigma(F_o^2)$. $^cR_w(F_o^2) = \{\sum [w(F_o^2 - F_c^2)^2] / \sum wF_o^4\}^{1/2}$. For $F_o^2 < 0$, $w = 1/[\sigma^2(F_o^2) + (mP)^2 + nP]$; where $P = (F_o^2 + 2F_c^2)/3$. Where m and n are 0.0383 and 0.6088 for 1, 0.0314 and 17.8241 for 4, 0.0167 and 38.1439 for 3, and 0.0363 and 79.4372 for 2, respectively.

product samples using Cu K α radiation (λ = 1.54 Å) on a PANalytical Empyrean X-ray diffractometer with a working voltage and an operating current of 45 kV and 40 mA, respectively. The measured data ranged from 5 to 75° using a step size increment of 0.013°. Analyses of the approximate chemical compositions of the crystals were probed using an energy-dispersive X-ray spectroscopy (EDX) study on a JEOL SEM 6010LA instrument at an accelerating voltage of 20 kV. Representative single crystals and powders were stuck onto a carbon tape adhesive for mounting to a sample pedestal. The elemental EDX data of selected crystals showed only Eu, Ag, IV (Sn or Ge), and Ch (S or Se) atoms in the approximate ratios of 1:2:1:4 and 3:2:2:8 as depicted in the Supporting Information in Figures S1–S4.

2.2.3. Solid-State UV–Vis–NIR Spectroscopy Methods. Room-temperature solid-state UV–vis–near-infrared (UV–vis–NIR) spectroscopy data for the polycrystalline samples of 1 to 4 were recorded in the form of reflectance data as a function of wavelength using a Shimadzu UV3600 instrument. The data were collected from 1000 nm (1.24 eV) to 250 nm (4.96 eV) using dried BaSO₄ as a reference. The reflectance data were converted to absorption data using the Kubelka–Munk equation: $\alpha/S = (1-R)^2/2R^{.43}$ Here, S, α , and R represent the scattering coefficient, absorption coefficient, and reflectance, respectively. The band gaps for the polycrystalline Eu₃Ag₂IV₂Ch₈ samples were calculated using the Tauc plot⁴³

$$(\alpha h \gamma)^n = A(h \gamma - E_{\sigma})$$

Here A, γ , h, and $E_{\rm g}$ are the proportionality constant, frequency of light, Planck's constant, and band gap, respectively. The n=1/2 and 2 values for the constant indicate the indirect and direct transitions, respectively.

2.2.4. Temperature-Dependent Magnetic Susceptibility. The magnetic susceptibility data of all of the polycrystalline samples were collected using a Quantum Design MPMS VSM squid instrument using a magnetic field of 10 T over a temperature range of 17–300 K. The polycrystalline samples were loaded separately into Gelatin capsules, and the capsules were then loaded inside a straw to collect the magnetic susceptibility data.

2.2.5. Second-Harmonic Generation (SHG) Measurements. Room-temperature mid-infrared (IR) SHG data were measured using a modified Kurtz–Perry system with a Ho:YAG laser at the wavelength of 2.09 μ m. ⁴⁴ The finely ground polycrystalline powders were sieved to 63–75 μ m and measured with AgGaS₂ (AGS) as the reference sample. A photomultiplier tube was used to collect the intensity of the frequency-doubled output data emitted from the sieved powdered samples.

2.2.6. Electronic Structure Calculations. Density functional theory methods were employed with the projector augmented wave method as implemented in the Vienna Ab Initio Simulation Package (VASP; ver. 6.4.2) for the electronic structure calculations of 1 to $4.^{45,46}$ Electron exchange and correlation were treated within the generalized gradient approximation of Perdew-Burke-Ernzerhof (PBE). Calculations were set with an energy convergence criterion of 10⁻⁸ eV/cell and an energy cutoff of 400 eV for the plane wave basis set, and using the PAW pseudopotentials for Eu (5s,5p,6s,4f,5d), Ag (5s,4d), Sn (4d,5s,5p), Ge (3d,4s,4p), Se (4s,4p), and S (3s,3p) in their respective structures. Their refined structures served as starting models for full geometry relaxation under the respective symmetry constraints until the norms on the atomic forces reached <0.01 eV Å-1. Site occupation disorder for the two Ag sites in the structures of 2, 3, and 4 were modeled as described previously for this structure type. 47 Next, spin-polarized density of states (DOS) calculations were performed using an $8 \times 8 \times 8$ k-point mesh (total: 75 k-points) for 1 and $4 \times 4 \times 4$ k-point meshes (total: 36 k-points) for 2 to 4. An effective on-site Coulomb interaction for the Eu 4f orbitals was approximated at 6 eV, consistent with prior literature.⁴⁸ Next, their spin-polarized band structures were calculated following the standard k-point paths of their respective crystal systems, 49 with either 10 (for 1) or 15 (for 2 to 4) k-point intersections along each Brillouin zone direction. For 1, this standard path came to a total of 90 k-points

along Γ -X-P-N- Γ -M-SIS₀- Γ |X-R| Γ -M, while for the structures of **2** to **4**, this consisted of a total of 90 k-points along Γ -H-N- Γ -P-H|P-N|. Individual contributions from the atomic orbitals were projected out as part of each calculation.

3. RESULTS AND DISCUSSION

3.1. Synthetic Investigations. Synthetic investigations of the Eu-Ag-IV-Ch (IV = Sn or Ge; Ch = S or Se) system, i.e., with one of four possible combinations of Ge:S, Ge:Sn, Sn:S, and Sn:Se, uncovered the first known quaternary chalcogenides combining the Eu(II) and Ag(I) cations. Each could potentially be attained having either the Eu-Ag₂-IV-Ch₄ or Eu₃-Ag₂-IV₂-Ch₈ compositions. The relative closeness of the two compositions led to the preferential formation of one of the two possible structures under these reaction conditions, such as the formation of the former composition only found for EuAg₂GeS₄ (1). Theoretically, this compound can be converted to the alternate compositions of compounds 2 to 4 via the following reaction: $EuAg_2GeS_4 + 2 EuS + GeS_2 \rightarrow$ Eu₃Ag₂Ge₂S₈. However, incomplete knowledge regarding the thermodynamically competing phases, as well as disorder over the Ag-site in the Eu₃-Ag₂-IV₂-Ch₈ structure (see below), currently prevents a more detailed probing of the relative energetic stabilities of the two compositions with respect to binaries/ternaries.

3.2. Structural Characterization by Single-Crystal XRD. High-temperature reactions at 1123 K produced $EuAg_2GeS_4$ (1) in the form of block-shaped yellow crystals in a yield of ~75%. A somewhat lower synthesis temperature of 1023 K produced a high-purity bulk powder of I that was found to be air-stable for at least 2 weeks. The structure of 1, shown in Figure 1, crystallizes in the noncentrosymmetric

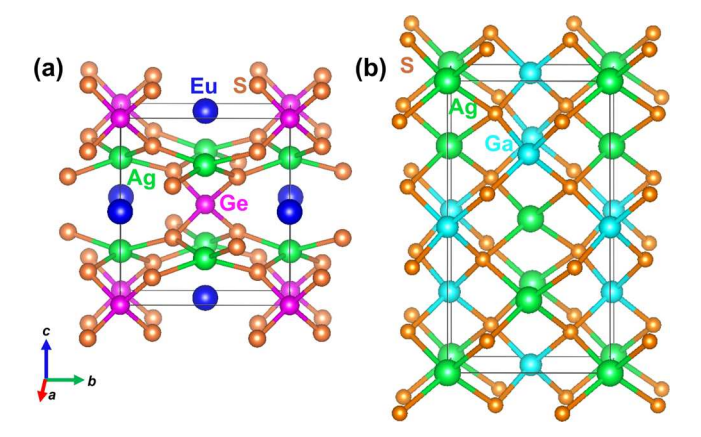


Figure 1. View of the unit cell of (a) $EuAg_2GeS_4$ (space group: $\overline{I42m}$) and (b) $AgGaS_2$ ($\overline{I42d}$) crystal structures approximately along the [100] direction.

 $I\overline{4}2m$ tetragonal space group with the unit cell dimension of a=6.8305(3) Å and c=7.5722(7) Å. Its structure contains a 3D $[Ag_2GeS_4]^{2-}$ network that is charge-balanced by Eu(II) cations within the cavities. This structure is related to the chalcopyrite-type structure, having a similar body-centered tetragonal cell as shown side-by-side in Figure 1b for $AgGaS_2$. Notably, the structure is a highly compressed version of the $AgGaS_2$ structure type, with the replacement of 1/2 of the Ag atoms by Ge and replacement of all of the Ga atoms on the unit-cell faces by Eu and Ag atoms, i.e., $AgGaS_2 \rightarrow (EuAg)(AgGe)S_4$ or written as $EuAg_2GeS_4$. Thus, the crystal structure of 1 can be

viewed as a substitutional variant of the parent, non-centrosymmetric, $AgGaS_2$ structure that maintains its breaking of the inversion symmetry. Briefly, the structure of 1 consists of layers of highly flattened AgS_4 tetrahedra, Figure 2a, that are

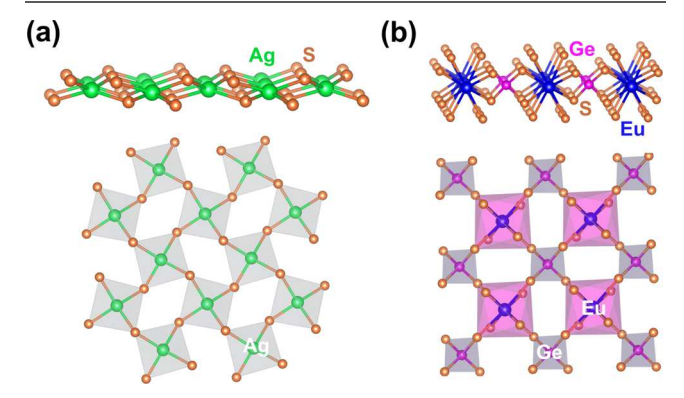


Figure 2. Structural views of the alternating layers of (a) vertex-sharing, flattened AgS_4 tetrahedra and (b) alternating, bridged, GeS_4 tetrahedra and EuS_8 polyhedral units in 1.

bridged by layers of more regular GeS_4 tetrahedra and Eu(II) cations, as shown in Figure 2b. The GeS_4 are all aligned, Figure S9, and thus break inversion symmetry. Condensation of these layers leads to the formation of a 3D $[Ag_2GeS_4]^{2-}$ network with Eu(II) cations within the cavities.

More locally, each GeS₄ tetrahedron shares vertices with eight adjacent AgS₄ tetrahedral units. Conversely, each AgS₄ flattened tetrahedron shares vertices with four adjacent AgS₄ tetrahedral units, Figure 2a, as well as four vertices with GeS₄ tetrahedral located above and below the layer. All four Ag–S and Ge–S distances are equivalent by symmetry, as listed in Table S3 for selected near-neighbor distances and angles. The Ag–S distance of 2.5700(6) Å can be compared with the Ag–S distances in isostructural compounds such as SrAg₂GeS₄ (2.5744(5) Å), ²² SrAg₂SiS₄ (2.5757(4) Å), ²² and BaAg₂GeS₄ (2.594(3) Å), ²³ whereas the Ge–S distances of 2.209(2) Å agree well with the Ge–S distances in SrAg₂GeS₄ (2.213(2) Å), ²² BaAg₂GeS₄ (2.210(4) Å), ²³ and BaCdGeS₄ (2.200(2)–2.238(1) Å). ⁵¹ The Eu–S distances varied from 3.139(2) Å to 3.244(2) Å, which is consistent with distances found in the previously reported EuCu₂SnS₄ (3.0497(8)–3.1444(6) Å), ³² EuCu₂SiS₄ (3.1013(8)–3.1655(9) Å), ²⁹ and α -EuZrS₃ (3.033(1)–3.290(1) Å). ⁵²

In contrast, high-temperature reactions for the other three Eu-Ag-IV-Ch combinations (i.e., IV:Ch = Ge:Se, Sn:Se, and Sn:S; 2, 3, and 4) each yielded red-colored crystals with the composition of Eu₃Ag₂IV₂Ch₈. Yields of the Eu₃Ag₂IV₂Ch₈ compounds varied from 60% to 80% and showed excellent stability in air for at least 2 weeks, as characterized by powder XRD. Their structures all crystallized in the cubic, noncentrosymmetric $\overline{143}d$ space group with the previously reported Sr₃Ag₂Ge₂Se₈ structure type.^{34,35} This complex structure, shown in Figure 3 for 3, can generally be described as the cubic-closest packing of SnSe₄ tetrahedra with additional tetrahedra filling all octahedral and tetrahedral sites, i.e., with 16 SnSe₄ tetrahedra per unit cell arranged as in the packing of a "Li₃Bi" parent type. As described above for I, the alignment of these tetrahedra breaks inversion symmetry. As listed in Table S5, the Ge-Se, Sn-Se, and Sn-S distances of 2, 3, and 4 range within comparable distances to those reported in prior studies, such as for $Ba_9Hf_3Sn_2Se_{19}$ (2.503(1)-2.541(1) Å), ¹⁸

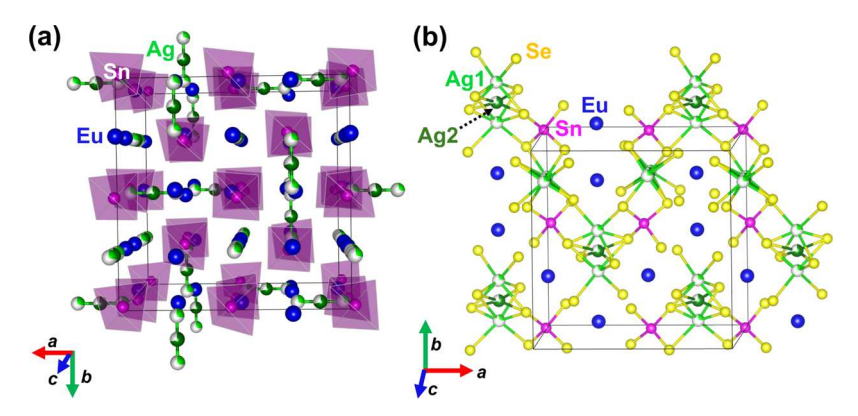


Figure 3. (a) Polyhedral view of the unit cell of 3, $Eu_3Ag_2Sn_2Se_8$, approximately along the *c*-axis direction with $SnSe_4$ tetrahedra in purple, the split position Ag-Ag distances in green, with the Se atoms not shown for clarity. (b) View of a (110) structural slice showing the local coordination environments of the split Ag1/Ag2 positions and all Ag-Se and Sn-Se bonds <3.45 Å.

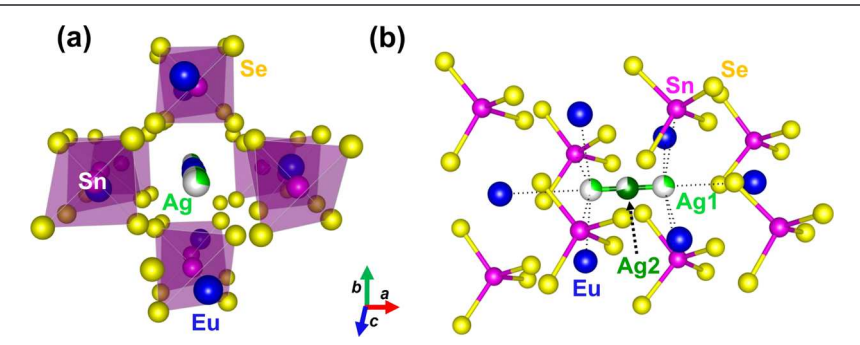


Figure 4. (a) Polyhedral view down a channel formed by neighboring $SnSe_4$ tetrahedra filled with Eu(II) and Ag(I) cations and (b) Ag1-Ag2-Ag1 "trimer" viewed horizontally with the shorter Ag1-Sn (~ 3.5 Å) and Ag1-Eu distances (~ 3.7 Å) labeled with dashed lines.

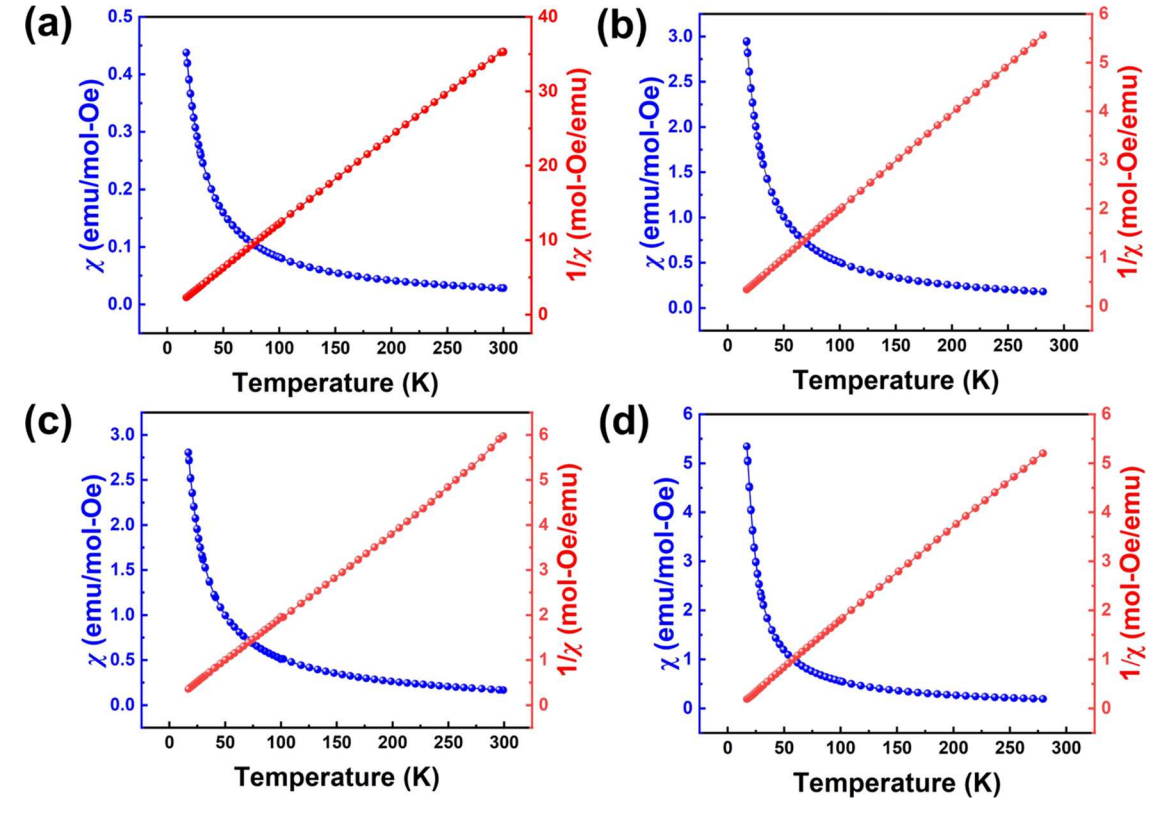


Figure 5. Plots of magnetic susceptibilities (χ ; blue) and inverse magnetic susceptibilities ($1/\chi$; red) versus temperature (K) for bulk crystalline powders of (a) 1 (EuAg₂GeS₄), (b) 2 (Eu₃Ag₂Ge₂Se₈), (c) 3 (Eu₃Ag₂Sn₂Se₈), and (d) 4 (Eu₃Ag₂Sn₂Se₈).

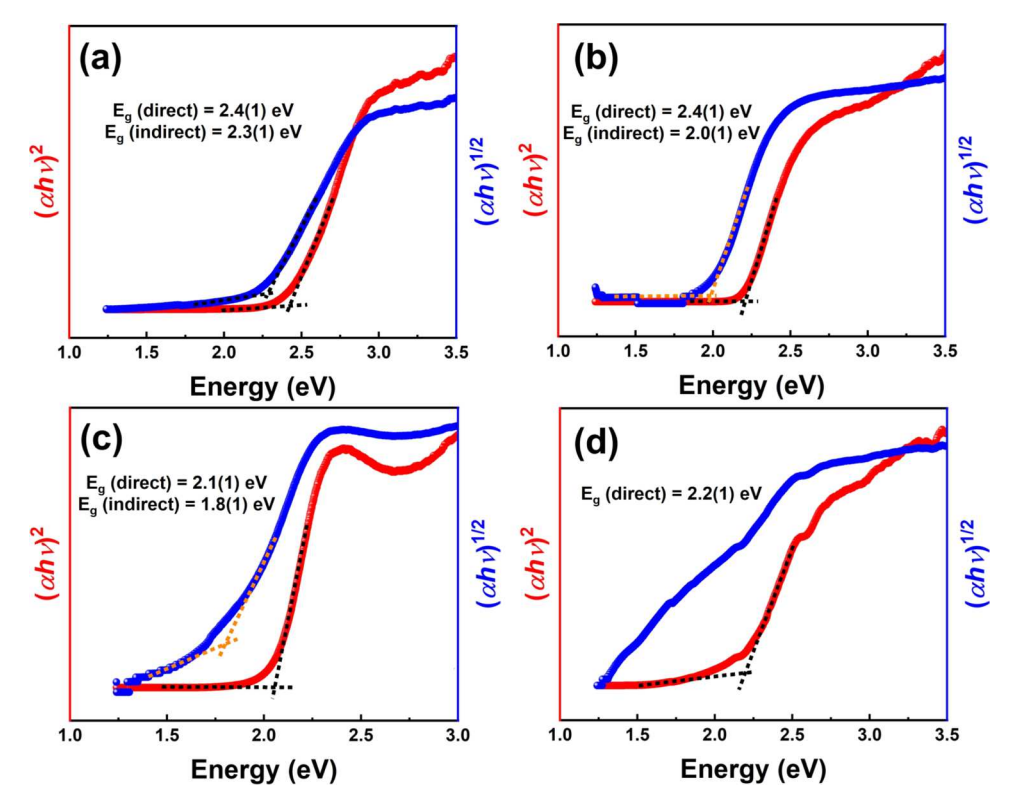


Figure 6. Tauc plots for the polycrystalline powders of (a) 1 (EuAg₂GeS₄), (b) 2 (Eu₃Ag₂Ge₂Se₈), (c) 3 (Eu₃Ag₂Sn₂Se₈), and (d) 4 (Eu₃Ag₂Sn₂Ss₈).

 $Ba_7Sn_3Se_{13}$ (2.477(1)–2.534(1) Å). 53 $BaCdGeSe_4$ (2.343(1)–2.392(1) Å), 54 $SrCdGeSe_4$ (2.327(2)–2.381(2) Å), 55 $BaCdSnS_4$ (2.353(1)–2.419(1) Å), and $Ba_3CdSn_2S_8$. 56 In contrast to 1, the structures of 2 to 4 contain two partially-occupied Ag positions Ag1 and Ag2 at the respective Wyckoff sites of 24d and 12a with different multiplicities. For each structure, the Ag1 and Ag2 sites consistently refined (with no constraints) to the respective occupancies of 0.31(1) and 0.71(1) for 2, 0.28(1) and 0.71(2) for 3, and 0.31(1) and 0.70(2) for 4, and thus the refined compositions of $Eu_3Ag_{1.99(1)}Ge_2Se_8$, $Eu_3Ag_{1.92(1)}Sn_2Se_8$, and $Eu_3Ag_{1.96(1)}Sn_2S_8$. These fall, within reasonable error, close to the nominal compositions for each based on charge-balancing and structural considerations, as described in further detail below.

Both the Ag and Eu cations are located within channels that are aligned down each of the symmetry-equivalent [100]/ [010]/[100] directions formed by the packing of the SnSe₄ tetrahedra, as labeled in Figure 3a and shown for a single channel in Figure 4. The Eu(II) cations coordinate as EuCh₈ polyhedra, as in 1, with respective Eu-Ch distances consistent with those found in $EuHfSe_3$ and other compounds. $^{57-59}$ The Ag2 atom is coordinated in a highly flattened AgSe₄ tetrahedral environment with Ag-Se distances of 2.6716(9) Å (\times 4), and bridges to four neighboring SnSe₄ tetrahedra to form its 3D network. Conversely, the split position for the Ag1 atom is located on opposing sides of each Ag2 site and is itself coordinated in a distorted octahedral environment, AgSe₆, with two short $(2.695(7) \text{ Å} (\times 2))$, and four longer Ag-Se distances $(3.319(1) \text{ Å } (\times 2); 3.402(1)\text{Å } (\times 2)). \text{ A view of the}$ condensation of the Ag1 and Ag2 polyhedra are shown together in Figure 3b. The short Ag1···Ag2 separation of ~1.4 to 1.6 Å in 2 to 4 precludes the simultaneous occupancy of both sites, i.e., with each "trimeric Ag1-Ag2-Ag1 cavity"

being occupied either by a central Ag2 or the opposing Ag1 positions. Consistent with this, their refined fractional occupancies sum to full occupancy, with the Ag2 site at ~70% and the Ag1 site at ~30% occupancy. Occupancy at the Ag1 site is less energetically favorable, with much shorter distances to three neighboring Eu(II) cations and two Sn(IV) cations, as labeled by dashed lines in Figure 4b. This raises the question of why the Ag1 position would be partially occupied? Considering a zero occupancy of the Ag1 site and a 100% occupancy of only the Ag2 site, the site multiplicity of 12 for the latter would render the compound electron-deficient. Conversely, a full occupancy of only the Ag1 site, at a higher multiplicity of 24, would yield excess electrons. Thus, the optimal charge balance of the framework is only attained by the mixed fractional occupancies of both the Ag1 and Ag2 sites, as is probed further in the magnetic data and the electronic structure calculations below.

3.3. Magnetic Susceptibilities. As a probe of the oxidation states of the Eu(II) cations in compounds 1 to 4, their temperature-dependent magnetic responses were measured as a function of temperature. The magnetic susceptibilities (χ) and inverse magnetic susceptibilities $(1/\chi)$ were plotted versus temperature in Figure 5. Each follows a paramagnetic behavior that could be fitted to the Curie-Weiss equation: $\gamma(T) = C/(T-\theta)$. Here, C and θ denote the Curie and Weiss constants, respectively. The plots of $1/\chi$ versus temperature were fairly linear over the entire temperature range and were fitted well within the temperature interval of 25 to 250 K. These fittings gave Curie-Weiss temperatures of -3.34, -0.35, -2.38, and 5.25 K for 1, 2, 3, and 4, respectively. These suggest weak antiferromagnetic (1 to 3) and ferromagnetic (4) interactions between the Eu cations, which are the only magnetic centers.

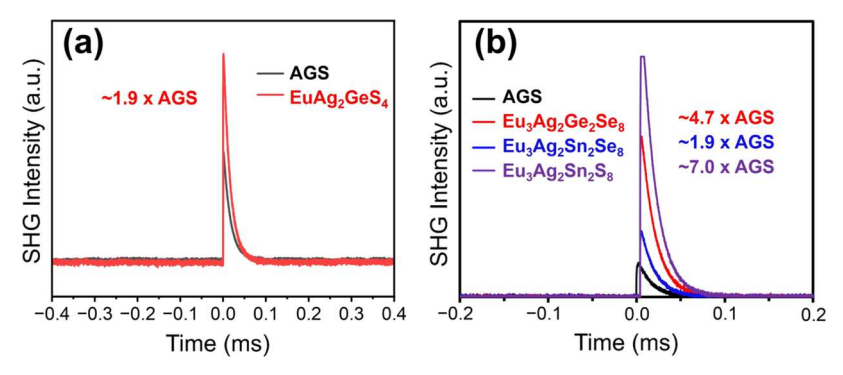


Figure 7. SHG responses versus AGS (black lines) for bulk powders of (a) $EuAg_2GeS_4$ (1) and (b) $Eu_3Ag_2Ge_2Se_8$ (2), $Eu_3Ag_2Sn_2Se_8$ (3), and $Eu_3Ag_2Sn_2Se_8$ (4).

The Eu cation is most commonly in either the $+2 (4f^7)$ and/ or +3 (4f°) oxidation states within metal chalcogenide compounds. The theoretical magnetic moments for the Eu(II) and Eu(III) cations are theoretically expected to be close to 7.94 and 6.93 μ B, respectively. The fitted, experimental magnetic moments per Eu atom were found to be 8.23 $\mu_{\rm B}$, 8.21 μ_B , 8.38 μ_B , and 8.36 μ_B , for 1, 2, 3, and 4, respectively, which is somewhat larger than the theoretical magnetic moment value (7.94 $\mu_{\rm B}$) for the Eu(II) cation. These slightly enhanced magnetic moments are comparable to many isoelectronic, e.g., Eu(II) and Gd(III), gadolinium containing compounds. From gadolinium magnetochemistry, it is well known that an increased moment can be ascribed to the gadolinium 5d electrons that induce 4f-5d exchange interactions. 60,61 Compounds with divalent europium cations are also known to show similar enhanced magnetic moments. 62 Thus, these magnetic moments are consistent with a Eu(II) oxidation state and with the divalent nature of the II-site cations in this structure type, as is known for Sr(II) and Pb(II) analogues in the reported Pb₃Ag₂Si₂S₈ and Sr₃Ag₂Sn₂S₈. The oxidation states of the Eu(II) cations are also further confirmed by the assigned oxidation states of Ag(I), Sn(IV)/ Ge(IV) in the chemical compositions as $(Eu^{2+})_3(Ag^{1+})_2(IV^{4+})_2(Ch^{2-})_8$ for 2 to 4.

3.4. Optical Properties and Electronic Structures. 3.4.1. Optical Band Gaps. Complex metal chalcogenides have represented attractive semiconductor candidates for optoelectronic-type applications owing to the versatility and tunability of their structures and properties. Within these and related structural families, this includes small visible-light band gaps, large optical absorption coefficients, high band dispersion, as well as functional defect tolerance. The optical band gaps of 1 to 4 were assessed using UV-vis diffuse reflectance spectroscopy on their polycrystalline powders at room temperature (300(2) K). Their respective Tauc plots were plotted, as shown in Figure 6a-d. The direct band transitions (red curves) for EuAg₂GeS₄, Eu₃Ag₂Ge₂Se₈, Eu₃Ag₂Sn₂Se₈, and Eu₃Ag₂Sn₂S₈ samples were estimated to be \sim 2.4 eV for 1 and 2, \sim 2.1 eV for 3, and \sim 2.2 eV for 4, consistent with the colors of their polycrystalline powders. Both 1 and 2 showed evidence for lower-energy indirect band gaps (blue curves) of ~2.3 and ~2.0 eV, respectively. The experimental direct and indirect band gaps of ~2.4 and ~2.3 eV, respectively, for the polycrystalline sample of 1 are slightly wider than the theoretically calculated direct and indirect transitions of 2.09 and 1.79 eV, respectively.³³ It is well known that theoretical calculations typically underestimate experimental band gaps. The band gap of 2 is wider than that previously reported for its

Sr-based analogue, Sr₃Ag₂Ge₂Se₈, at ~1.90 eV. By contrast, both Sn(IV)-containing compounds exhibited onsets of indirect transitions that were relatively ambiguous, extending to ~1.5 eV and below. Prior studies in the II₃-I₂-IV₂-Ch₈ chemical family show that related compounds typically exhibit indirect band gaps that are lower in energy by only ~0.1 eV or less than kT ("quasi-direct") than the direct transitions, 47 which would also be consistent with the results of electronic structure calculations for 2 to 4 (described below). Taken together, this suggests that their indirect transitions have likely been obscured by impurities and/or a high degree of structural disorder in the Sn(IV)-containing chalcogenides. Also generally, the Eu(II)-containing compounds exhibit somewhat smaller band gaps than their Sr-based versions. For example, the quasi-direct band gap of the Sr-analogue to 4, i.e., $Sr_3Ag_2Sn_2S_8$, is reported to be higher in energy at ~2.66 eV.

3.4.2. Second-Harmonic Generation (SHG) Activities. Complex metal chalcogenides with chalcopyrite and related structure types with tetrahedral network motifs have also been demonstrated to have among the largest SHG responses and laser-induced damage threshold (LIDT) for infrared nonlinear optical applications. Prior research has shown that effective strategies to enhance these properties have included (a) the incorporation of rare-earth elements, such as in the cases of Eu₂P₂S₆ and Dy₃GaS₆ which have 3.4× and 14× the LIDT at 1.064 μ m, ^{17,18} and (b) targeted co-substitutions of alkali or alkaline earth metals with main-group metal cations such as Sn(IV) and Ge(IV) to increase the band gap and inhibit multiphoton absorptions, such as known in Na₂BaSnS₄ (E_g = 3.27 eV) versus AgGaS₂ (2.56 eV). ^{19,20}

The four quaternary chalcogenides, EuAg₂GeS₄ (1), Eu₃Ag₂Ge₂Se₈, (2) Eu₃Ag₂Sn₂Se₈ (3), and Eu₃Ag₂Sn₂Ss₈ (4), represent a potentially effective combination of these strategies. Using a modified Kurtz–Perry method, ⁴⁴ the SHG activities as powders exhibited remarkably high responses of ~1.9, ~4.7, ~1.9, and ~7 (×AGS) at 2.09 μ m, as plotted in Figure 7. Their LIDT was not measured directly. However, the LIDT of each compound is significantly larger than that of AGS as evidenced by the lack of signal decay and sample destruction over the duration of the measurement. By comparison to other metal chalcogenides containing a single anion, as listed in Table 2, these currently represent some of the largest known responses.

Among an even wider range of noncentrosymmetric materials that contain multiple anions, only a handful have elicited SHG responses this large at this wavelength, such as $Ba_3CsGa_5Se_{10}Cl_2$ and $Ba_3ZnGa_5Se_{10}Cl_2$ (100 and 59 \times AGS, respectively) 66,67 or $K_2P_2Se_6$ ($\sim\!150$ \times AGS). 68 Interestingly, there is also a small family of compounds with a similar

Table 2. Selected List of Currently Known Metal Chalcogenides (Single Anion) Exhibiting High SHG Activity

compound	space group	$E_{\rm g}$ (eV)	SHG ^a	references
AgGaS ₂	$I\overline{4}2d$	2.54-2.73	1.00	63
Dy ₃ GaS ₆	$Cmc2_1$	2.81	0.2 × KTP @1.91 μm	18
Na ₂ BaSnS ₄	$I\overline{4}2d$	3.27	0.5	19
$\text{Li}_2\text{Ba}_7\text{Sn}_4\text{S}_{16}$	I 4 3d	2.30	0.5	63
Li ₂ Ba ₆ MnSn ₄ S ₁₆	I 4 3d	2.76	5.1	64
EuCdGeSe ₄	Ama2	2.25	3.8	65
SrAg ₂ GeS ₄	$I\overline{4}2m$	1.73	\sim 0.62 × AGS 1.8 μ m	22
SrAg ₂ SiS ₄	$\overline{142m}$	2.08	\sim 0.59 × AGS 1.8 μ m	22
EuCu ₂ GeS ₄	$P3_{2}21$	2.32	not active	29
EuCu ₂ SiS ₄	$P3_{2}21$	2.36	not active	29
BaLi ₂ GeS ₄	$I\overline{4}2m$	3.66	~0.5	20
$BaLi_2SnS_4$	$I\overline{4}2m$	3.07	~0.7	20
EuAg ₂ GeS ₄	$\overline{142m}$	2.4	~1.9 × AGS @2.1 µm	this work
Eu ₃ Ag ₂ Ge ₂ Se ₈	I 4 3d	2.0	~4.7 × AGS @2.1 µm	this work
$Eu_{3}Ag_{2}Sn_{2}Se_{8}$	I 4 3d	<2.0	~1.9 × AGS @2.1 µm	this work
Eu ₃ Ag ₂ Sn ₂ S ₈	I 4 3d	<2.0	~7.0 × AGS @2.1 μm	this work

^aSHG values are listed in units of ×AGS (d_{ij} = 11 pm/V) and @2.09 μ m unless otherwise stated.

structure to compounds **2** to **4**, $A_2Ba_7Sn_4Ch_{16}$ (A = Na, Li, Ch = S, Se). These compounds contain similar networks of SnCh₄ tetrahedra connected via (A/Ba)Ch₄ tetrahedra and Ba atoms within the tunnels. Despite the similar structures and optical band gaps of $A_2Ba_7Sn_4Ch_{16}$ to compounds **2** to **4**, the SHG responses are smaller (0.1–0.5 × AGS). While **2**, **3**, and

4 exhibit large SHG responses, currently there are few structural and compositional conclusions that can be immediately drawn. The mid-infrared SHG response of the EuAg₂GeS₄ sample, Figure 7a, was found to be $\sim 1.9 \times AGS$ @ 2090 nm and can be compared to the previously reported compounds listed in Table 2. As the EuAg₂GeS₄ structure is related to the commercially available NLO material AgGaS₂ (chalcopyrite) and the band gap of 2.4(1) eV is very close to the band gap of AGS (2.62 eV), the NLO properties of EuAg₂GeS₄ are promising. Compounds 1–4 are thus interesting for further investigation into the electronic origins of their optical properties to better understand their large SHG coefficients, as analyzed below using electronic structure calculations.

3.4.3. Electronic Structure Calculations. The electronic structures of metal chalcogenides have been explored in prior studies for a deeper understanding of their optoelectronic properties, such as their band gap edges and energetic separation, conduction band (CB) and valence band (VB) dispersion, effective masses of electrons ($m_{\rm e}$) and holes ($m_{\rm h}$), and tolerance to structural defects. Thus, 1 and the isostructural series of 2 to 4 represent an opportunity to examine the origins of their optoelectronic properties, including an initial assessment of potential relationships with their SHG activities. Electronic structures of several compounds that fall within the II–I₂-IV-Ch₄ and II₃–I₂-IV₂–Ch₈ (Ch = S or Se) chemical families have been reported, ^{22,47} such as the electronic structure of 1.³³

Density functional theory calculations were performed on the fully geometry-relaxed structures of compounds 1 to 4, including their spin-polarized density of states (DOS) and band structures with the individual atomic orbital contributions projected out. The results for the isostructural series of 2 to 4 are plotted together in Figure 8, while the results for 1 are provided in Figure 9. To begin with the isostructural series, the

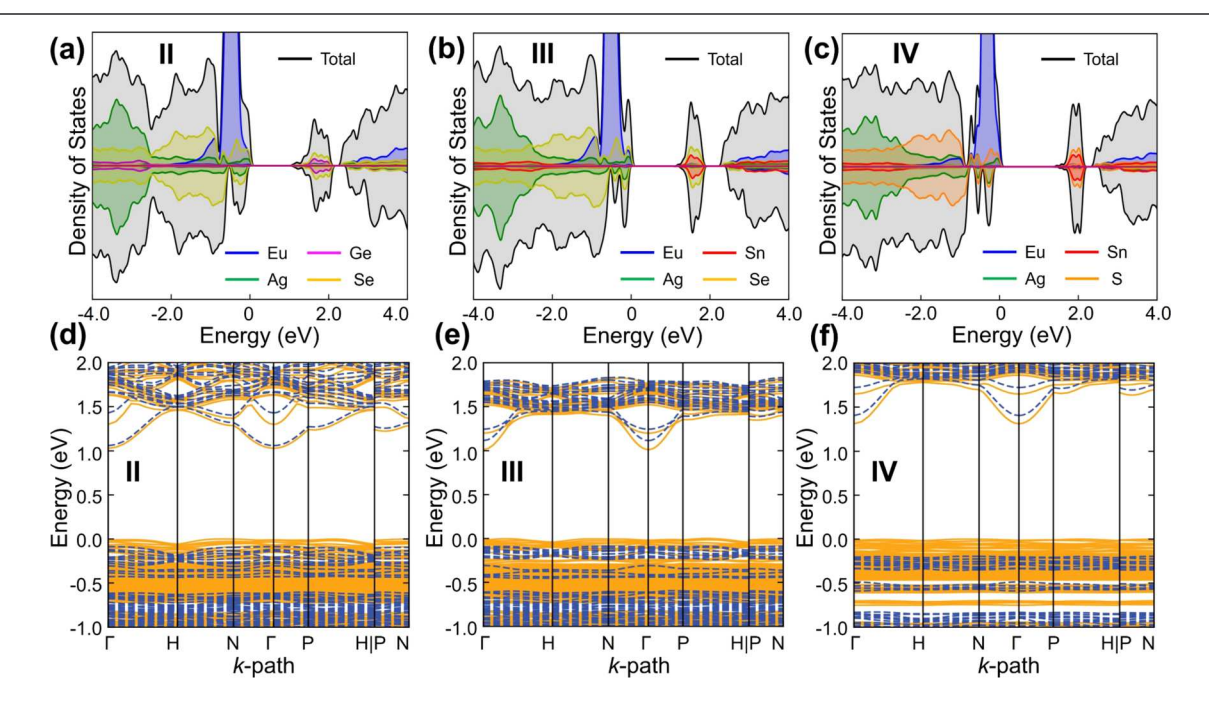


Figure 8. Calculated spin-polarized density of states (DOS; top) and band structures (bottom) for $Eu_3Ag_2Ge_2Se_8$ (2; a, d), $Eu_3Ag_2Sn_2Se_8$ (3; b, e), and $Eu_3Ag_2Sn_2Se_8$ (4; c, f), with the Fermi level at 0 eV, the atomic orbital contributions labeled with colored lines, and the spin-polarized bands labeled as up (yellow, solid) and down (blue, dashed).

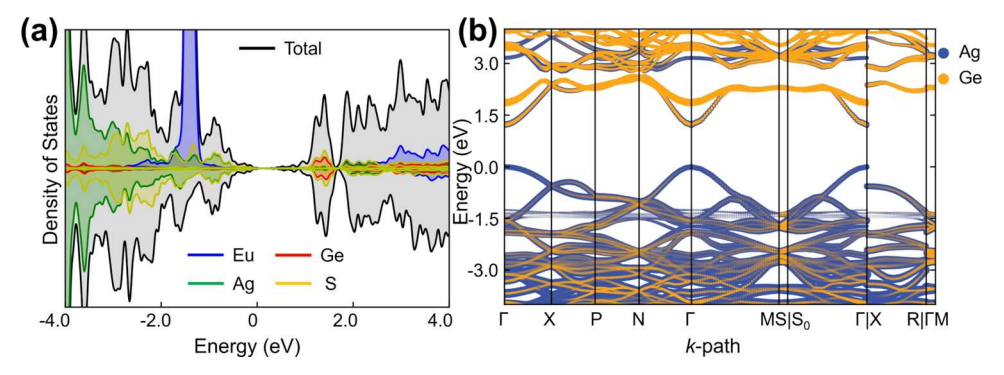


Figure 9. Calculated spin-polarized density of states (DOS; a) and band structure (b) for $EuAg_2GeS_4$ (1) with the Fermi level at 0 eV, the atomic orbital contributions labeled with colored lines.

VB and CB edges of each originate from the filled Ag(4d)-S/ Se(3p/4p) states and empty Ge/Sn(4p/5p)-S/Se(3p/4p)based states, respectively. In 3, for example, these contributions correspond to the Ag-/Se-based and Sn-/Se-based states at the VB and CB edges. However, in each case, the half-filled Eu(II) 4f⁷ states also significantly contribute to a highly localized band (blue line) near the valence band edges. The Eu-based states shift closer to the VB edge in the order of 3 < 2 < 4 with a corresponding decrease in the VB dispersion in that order, as illustrated in Figure 8. Upon reaching compound 4, for example, the Eu 4f⁷ states correspond to the predominant contributions at the VB edge, with the Ag- and S-based states constituting the minor contributions. Iso-surface plots of the electron density near (~0.5 to 0.3 eV) the VB edges are illustrated in Figures S12-S14 in the Supporting Information. Across this series of increasing Eu contributions, i.e., from 3 to 2 to 4, the calculated effective hole masses are -2.8, -3.2, and $-5.8 m_e$. Notably, this trend with increasing Eu 4f⁷ contributions at the VB edge is positively correlated with the SHG activity from \sim 1.9 to \sim 4.7 to \sim 7 × AGS for 3 to 2 to 4. This is consistent with prior theoretical studies that show higher SHG activity arising from flatter bands as well as from contributions from more polarizable cations at the band edges.⁶⁹ Further, calculations predict "quasi-direct" band gaps for each, with the indirect band gaps only minimally smaller (~0.01 to 0.02 eV) than the higher-energy direct band transitions.

Similarly for 1 (EuAg₂GeS₄), its electronic structure shows VB and CB edges stemming, respectively, from filled Ag(4d)-S(3p) states and empty Ge(4p)-S(3p), as plotted in Figure 9. The electron density of the VB edge is clearly two-dimensional in nature, with the greatest degree of band dispersion along the flattened AgS₄-type layers. The CB states show a similarly high band dispersion across the GeS4 tetrahedra but also show a small admixture from the Ag(4d) states throughout the network, most especially near the lowest CB edges seen in the band structure. Consistent with prior reports in the II-I₂-IV-Ch₄ family, the effective masses of carriers at both the CB and VB edges are relatively small at 0.22 m_e and -0.38 m_h respectively. Further, the Eu 4f⁷-based states are buried more deeply within the valence band, at ~1.5 eV below the Fermi level, as compared to compounds 2 to 4. Its SHG activity is among the smallest of the series, consistent with the trend described above. This trend is also consistent with the absence of significant SHG activity in the prior Eu(II)-based chalcogenides forming in this structure type, e.g., as reported for Li₂EuGeS₄ and Cu₂EuSnSe₄. Further experimental and

theoretical research is ongoing to understand more deeply this relationship between SHG and the electronic structures of Eu(II)-based chalcogenides.

4. CONCLUSIONS

In conclusion, synthetic investigations of the Eu-Ag-IV-Ch (IV = Sn or Ge; Ch = S or Se) systems have unveiled four new Eu(II)-based quaternary chalcogenides that are noncentrosymmetric and exhibit large mid-IR SHG activities. The four new compounds, EuAg₂GeS₄ (1), Eu₃Ag₂Ge₂Se₈ (2) Eu₃Ag₂Sn₂Se₈ (3), and Eu₃Ag₂Sn₂S₈ (4), consist of body-centered arrangements of oriented (Ge/Sn)Ch₄ tetrahedra that break inversion symmetry. These tetrahedra are bridged together by highly flattened AgCh₄ tetrahedra into 3D networks, i.e., [Ag₂GeS₄]²⁻ or $[Ag_2IV_2Ch_8]^{6-}$, and charge-balanced by the Eu(II) cations. Measured optical band gaps occurred over visible-light energies and ranged from ~2.3 eV for the yellow crystals of 1 and ~2.0 to 1.8 eV for the red crystals of 2, 3, and 4. Spin-polarized band structure calculations found that their valence band (VB) and conduction band (CB) edge states stem from interactions of the filled Ag-to-S/Se and empty Ge/Sn-to-S/Se-based states, respectively. However, an apparent shift of the Eu(II) 4f⁷based to the valence band edge occurred in the order of 1 < 3< 2 < 4 and positively correlated with the increasing SHG activity, which ranged from a large ~1.9 × AGS (AgGaS₂) for 1, to remarkably high values of \sim 1.9 for 3, \sim 4.7 for 2, and \sim 7 (XAGS) for 4. Thus, these results represent some of the highest attained SHG properties within new Eu(II)-based chalcogenides that, in turn, inform future potential design strategies for the development of advanced, functional NLO materials.

ASSOCIATED CONTENT

Supporting Information

The Supporting Information is available free of charge at https://pubs.acs.org/doi/10.1021/acs.chemmater.4c01885.

SEM data of the elemental composition and mapping; PXRD data; atomic displacement parameters; and metric details of the final refined structure (PDF)

Accession Codes

The crystallographic data files of $EuAg_2GeS_4$, $Eu_3Ag_2Ge_2Se_8$, $Eu_3Ag_2Sn_2Se_8$, and $Eu_3Ag_2Sn_2S_8$ structures are submitted to Cambridge Crystallographic Data Centre (CCDC) with the CCDC numbers of 2356431, 2342594, 2342593, and 2342595, respectively, and can be accessed from CCDC (https://www.ccdc.cam.ac.uk/) at no charge.

AUTHOR INFORMATION

Corresponding Author

Paul A. Maggard — Department of Chemistry, North Carolina State University, Raleigh, North Carolina 27695, United States; orcid.org/0000-0002-3909-1590; Email: Paul Maggard@ncsu.edu

Authors

Subhendu Jana – Department of Chemistry, North Carolina State University, Raleigh, North Carolina 27695, United States

Eric A. Gabilondo – Department of Chemistry, University of Houston, Houston, Texas 77204, United States;
ocid.org/0000-0001-5509-273X

Machima Mongkhonratanachai – Department of Chemistry, North Carolina State University, Raleigh, North Carolina 27695, United States

Yujie Zhang — Department of Chemistry, University of Houston, Houston, Texas 77204, United States

P. Shiv Halasyamani — Department of Chemistry, University of Houston, Houston, Texas 77204, United States;
orcid.org/0000-0003-1787-1040

Complete contact information is available at: https://pubs.acs.org/10.1021/acs.chemmater.4c01885

Notes

The authors declare no competing financial interest.

ACKNOWLEDGMENTS

The authors acknowledge primary support of this work from the National Science Foundation (DMR-2317605). Single-crystal X-ray characterization was performed in part by the Molecular Education, Technology and Research Innovation Center (METRIC) at NC State University, which is supported by the State of North Carolina. Provision of computing resources is also acknowledged as provided by the North Carolina State University High Performance Computing Services Core Facility (RRID:SCR_022168). E.G., Y.Z., and P.S.H. thank the Welch Foundation (E-1457) and the National Science Foundation (DMR-2002319) for support.

■ REFERENCES

- (1) Garmire, E. Nonlinear Optics in Daily Life. Opt. Express 2013, 21 (25), 30532–30544.
- (2) Luo, X.; Li, Z.; Guo, Y.; Yao, J.; Wu, Y. Recent Progress on New Infrared Nonlinear Optical Materials with Application Prospect. *J. Solid State Chem.* **2019**, *270*, *674*–*687*.
- (3) Pushkarsky, M. B.; Webber, M. E.; Macdonald, T.; Patel, C. K. N. High-Sensitivity, High-Selectivity Detection of Chemical Warfare Agents. *Appl. Phys. Lett.* **2006**, *88* (4), No. 044103.
- (4) Tholl, H. D. In Review and Prospects of Optical Countermeasure Technologies, Technologies for Optical Countermeasures XV; SPIE, 2018.
- (5) Schunemann, P. G.; Schepler, K. L.; Budni, P. A. Nonlinear Frequency Conversion Performance of AgGaSe₂, ZnGeP₂, and CdGeAs₂. MRS Bull. 1998, 23 (7), 45–49.
- (6) He, J.; Iyer, A. K.; Waters, M. J.; Sarkar, S.; Zu, R.; Rondinelli, J. M.; Kanatzidis, M. G.; Gopalan, V. Giant Non-Resonant Infrared Second Order Nonlinearity in γ -NaAsSe₂. Adv. Opt. Mater. **2022**, 10 (2), No. 2101729.
- (7) Bera, T. K.; Jang, J. I.; Song, J.-H.; Malliakas, C. D.; Freeman, A. J.; Ketterson, J. B.; Kanatzidis, M. G. Soluble Semiconductors $AASSe_2$ (A = Li, Na) with a Direct-Band-Gap and Strong Second Harmonic

- Generation: A Combined Experimental and Theoretical Study. J. Am. Chem. Soc. 2010, 132 (10), 3484–3495.
- (8) Chung, I.; Kanatzidis, M. G. Metal Chalcogenides: A Rich Source of Nonlinear Optical Materials. *Chem. Mater.* **2014**, 26 (1), 849–869.
- (9) Wu, H.; Yu, H.; Yang, Z.; Hou, X.; Su, X.; Pan, S.; Poeppelmeier, K. R.; Rondinelli, J. M. Designing a Deep-Ultraviolet Nonlinear Optical Material with a Large Second Harmonic Generation Response. *J. Am. Chem. Soc.* **2013**, *135* (11), 4215–4218.
- (10) Tran, T. T.; Yu, H.; Rondinelli, J. M.; Poeppelmeier, K. R.; Halasyamani, P. S. Deep Ultraviolet Nonlinear Optical Materials. *Chem. Mater.* **2016**, 28 (15), 5238–5258.
- (11) Liao, J.-H.; Marking, G. M.; Hsu, K. F.; Matsushita, Y.; Ewbank, M. D.; Borwick, R.; Cunningham, P.; Rosker, M. J.; Kanatzidis, M. G. α and β -A₂Hg₃M₂S₈ (A = K, Rb; M = Ge, Sn): Polar Quaternary Chalcogenides with Strong Nonlinear Optical Response. *J. Am. Chem. Soc.* **2003**, 125, 9484–9493.
- (12) Sun, M.; Xing, W.; Chen, S. K.; Li, C.; Liu, W.; Lee, M.-H.; Yao, J. $ACd_4Ga_5Te_{12}$ (A = K, Rb, Cs): Tellurides with a Strong Nonlinear Optical Response and Purple Emission. *Chem. Mater.* **2023**, 35, 7218–7228.
- (13) Iyer, A. K.; Cho, J. B.; Waters, M. J.; Cho, J. S.; Oxley, B. M.; Rondinelli, J. M.; Jang, J. I.; Kanatzidis, M. G. Ba₂MAsQ₅ (Q = S and Se) Family of Polar Structures with Large Second Harmonic Generation and Phase Matchability. *Chem. Mater.* **2022**, *34*, 5283–5293.
- (14) Greaney, M. A.; Ramanujachary, K. V.; Teweldemedhin, Z.; Greenblatt, M. Studies on the Linear Chain Antiferromagnets: Ba_2MnX_3 (X = S, Se, Te) and Their Solid Solutions. *J. Solid State Chem.* **1993**, 107, 554–562.
- (15) Jana, S.; Gabilondo, A.; McGuigan, S.; Maggard, P. A. Syntheses, Crystal Structures, and Electronic Structures of New Quaternary Group-IV Selenide Semiconductors. *Inorg. Chem.* **2024**, 63, 6474–6482.
- (16) Zhao, L.-D.; Lo, S.-H.; Zhang, Y.; Sun, H.; Tan, G.; Uher, C.; Wolverton, C.; Dravid, V. P.; Kanatzidis, M. G. Ultralow Thermal Conductivity and High Thermoelectric Figure of Merit in SnSe Crystals. *Nature* **2014**, *508*, 373–377.
- (17) Guo, S.-P.; Chi, Y.; Guo, G.-C. Recent Achievements on Middle and Far-Infrared Second-Order Nonlinear Optical Materials. *Coord. Chem. Rev.* **2017**, 335, 44–57.
- (18) Zhang, M.-J.; Li, B.-X.; Liu, B.-W.; Fan, Y.-H.; Li, X.-G.; Zeng, H.-Y.; Guo, G.-C. $\operatorname{Ln_3GaS_6}$ (Ln = Dy, Y): New Infrared Nonlinear Optical Materials with High Laser Induced Damage Thresholds. *Dalton Trans.* **2013**, 42, 14223–14229.
- (19) Wu, K.; Yang, Z.; Pan, S. Na_2BaMQ_4 (M = Ge, Sn; Q = S, Se): Infrared Nonlinear Optical Materials with Excellent Performances and That Undergo Structural Transformations. *Angew. Chem., Int. Ed.* **2016**, 55, 6713–6715.
- (20) Wu, K.; Zhang, B.; Yang, Z.; Pan, S. New Compressed Chalcopyrite-like Li₂BaM^{IV}Q₄ (M^{IV} = Ge, Sn; Q = S, Se): Promising Infrared Nonlinear Optical Materials. *J. Am. Chem. Soc.* **2017**, *139*, 14885–14888.
- (21) Yang, Y.; Wu, K.; Wu, X.; Zhang, B.; Gao, L. A new family of quaternary thiosilicates SrA_2SiS_4 (A = Li, Na, Cu) as promising infrared nonlinear optical crystals. *J. Mater. Chem. C* **2020**, 8, 1762–1767.
- (22) Wessler, G. C. M.; Wang, T.; Sun, J.-P.; Liao, Y.; Fischer, M. C.; Blum, V.; Mitzi, D. B. Structural, Optical, and Electronic Properties of Two Quaternary Chalcogenide Semiconductors: Ag₂SrSiS₄ and Ag₂SrGeS₄. *Inorg. Chem.* **2021**, *60*, 12206–12217.
- (23) Chen, H.; Liu, P.-F.; Li, B.-X.; Lin, H.; Wu, L.-M.; Wu, X.-T. Experimental and theoretical studies on the NLO properties of two quaternary non-centrosymmetric chalcogenides: BaAg₂GeS₄ and BaAg₂SnS₄. *Dalton Trans.* **2018**, *47*, 429–437.
- (24) Nian, L.; Wu, K.; He, G.; Yang, Z.; Pan, S. Effect of Element Substitution on Structural Transformation and Optical Performances in $I_2BaM^{IV}Q_4$ (I = Li, Na, Cu, and Ag; MIV = Si, Ge, and Sn; Q = S and Se). *Inorg. Chem.* **2018**, *57* (6), 3434–3442.

- (25) Aitken, J. A.; Larson, P.; Mahanti, S. D.; Kanatzidis, M. G. Li₂PbGeS₄ and Li₂EuGeS₄: Polar Chalcopyrites with a Severe Tetragonal Compression. *Chem. Mater.* **2001**, *13*, 4714–4721.
- (26) Nian, L.; Huang, J.; Wu, K.; Su, Z.; Yang, Z.; Pan, S. $BaCu_2M^{IV}Q_4$ ($M^{IV}=Si$, Ge, and Sn; Q=S, Se): Synthesis, Crystal Structures, Optical Performances and Theoretical Calculations. *RSC Adv.* **2017**, *7*, 29378–29385.
- (27) Teske, C. L. Darstellung und Kristallstruktur von Cu₂SrSnS₄. Z. Anorg. Allg. Chem. **1976**, 419, 67–76.
- (28) Teske, C. L. Über Die Darstellung Und Röntgenographische Untersuchung von Cu₂SrGeS₄ Und Cu₂BaGeS₄. Z. Naturforsch. B 1979, 34, 386–389.
- (29) Sun, Z.-D.; Chi, Y.; Guo, S.-P. Cu_2EuMQ_4 (M=Si, Ge; Q=S, Se): Syntheses, Structure Study and Physical Properties Determination. *J. Solid State Chem.* **2019**, 269, 225–232.
- (30) Sarkar, A.; Viswanathan, G.; Wu, K.; Miller, G. J.; Kovnir, K. BaCu₂SiS₄: A New Member of the A^{II}B₂^IM^{IV}Q₄ Chalcogenide Family with a Chiral Crystal Structure. *Z. Anorg. Allg. Chem.* **2023**, *649*, No. e202300147.
- (31) Yang, Y.; Wu, K.; Zhang, B.; Wu, X.; Lee, M.-H. Infrared Nonlinear Optical Polymorphs α and β -SrCu₂SnS₄ Exhibiting Large Second Harmonic Generation Responses with Requisite Phase-Matching Behavior. *Chem. Mater.* **2020**, 32, 1281–1287.
- (32) Aitken, J. A.; Lekse, J. W.; Yao, J.-L.; Quinones, R. Synthesis, Structure and Physicochemical Characterization of a Noncentrosymmetric, Quaternary Thiostannate: EuCu₂SnS₄. *J. Solid State Chem.* **2009**, *182*, 141–146.
- (33) Wang, T.; McWhorter, T. M.; Wessler, G. C. M.; Yao, Y.; Song, R.; Mitzi, D. B.; Blum, V. Exploration, Prediction, and Experimental Verification of Structure and Optoelectronic Properties in I_2 -Eu-IV- X_4 (I = Li, Cu, Ag; IV = Si, Ge, Sn; X = S, Se) Chalcogenide Semiconductors. *Chem. Mater.* **2024**, *36*, 340–357.
- (34) Yang, Y.; Song, M.; Zhang, J.; Gao, L.; Wu, X.; Wu, K. Coordinated Regulation on Critical Physiochemical Performances Activated from Mixed Tetrahedral Anionic Ligands in New Series of $\mathrm{Sr}_6\mathrm{A}_4\mathrm{M}_4\mathrm{S}_{16}$ (A = Ag, Cu; M = Ge, Sn) Nonlinear Optical Materials. *Dalton Trans.* **2020**, 49, 3388–3392.
- (35) Tampier, M. Chalkogenogermanate Der Übergangselemente Mit Unedlen Metallen Heinrich-Heine-Universität Düsseldorf: Germany, 2002
- (36) Bruker APEX4 Version .5-1 Data Collection and Processing Software; Bruker Analytical X-Ray Instruments, Inc.: Madison, WI, 2009
- (37) Sheldrick, G. M. SADABS; Bruker AXS, Inc.: Madison, Wisconsin, USA, 2008.
- (38) Sheldrick, G. M. XPREP, version 2008/2; Bruker AXS Inc.: Madison, 2018.
- (39) Sheldrick, G. M. A Short History of SHELX. Acta Crystallogr., Sect. A: Found. Crystallogr. 2008, 64 (1), 112–122.
- (40) Sheldrick, G. M. Crystal Structure Refinement with SHELXL. Acta Crystallogr., Sect. C: Struct. Chem. 2015, 71, 3-8.
- (41) Spek, A. L. Single-Crystal Structure Validation with the Program PLATON. *J. Appl. Crystallogr.* **2003**, *36*, 7–13.
- (42) Gelato, L. M.; Parthé, E. STRUCTURE TIDY a Computer Program to Standardize Crystal Structure Data. *J. Appl. Crystallogr.* **1987**, *20*, 139–143.
- (43) Makuła, P.; Pacia, M.; Macyk, W. How To Correctly Determine the Band Gap Energy of Modified Semiconductor Photocatalysts Based on UV–Vis Spectra. *J. Phys. Chem. Lett.* **2018**, *9*, 6814–6817.
- (44) Kurtz, S. K.; Perry, T. T. A Powder Technique for the Evaluation of Nonlinear Optical Materials. *J. Appl. Phys.* **1968**, 39, 3798–3813.
- (45) Kresse, G.; Furthmüller, J. Efficient Iterative Schemes for *Ab Initio* Total-Energy Calculations Using a Plane-Wave Basis Set. *Phys. Rev. B* **1996**, *54*, 11169–11186.
- (46) Kresse, G.; Furthmüller, J. Efficiency of Ab-Initio Total Energy Calculations for Metals and Semiconductors Using a Plane-Wave Basis Set. *Comput. Mater. Sci.* 1996, 6, 15–50.

- (47) McKeown Wessler, G. C.; Wang, T.; Blum, V.; Mitzi, D. B. Cubic Crystal Structure Formation and Optical Properties within the Ag-B^{II}-M^{IV}-X (B^{II} = Sr, Pb; M^{IV} = Si, Ge, Sn; X = S, Se) Family of Semiconductors. *Inorg. Chem.* **2022**, *61*, 2929–2944.
- (48) Yu, M.; Yang, S.; Wu, C.; Marom, N. Machine Learning the Hubbard *U* Parameter in DFT+*U* Using Bayesian Optimization. *npj Comput. Mater.* **2020**, *6*, No. 180.
- (49) Hinuma, Y.; Pizzi, G.; Kumagai, Y.; Oba, F.; Tanaka, I. Band Structure Diagram Paths Based on Crystallography. *Comput. Mater. Sci.* **2017**, *128*, 140–184.
- (50) Hobden, M. V. Optical Activity in a Non-Enantiomorphous Crystal: AgGaS₂. Acta Crystallogr., Sect. A: Cryst. Phys., Diffr., Theor. Gen. Crystallogr. 1968, 24, 676–680.
- (51) Lin, Y.-J.; Ye, R.; Yang, L.-Q.; Jiang, X.-M.; Liu, B.-W.; Zeng, H.-Y.; Guo, G.-C. BaMnSnS₄ and BaCdGeS₄: Infrared Nonlinear Optical Sulfides Containing Highly Distorted Motifs with Centers of Moderate Electronegativity. *Inorg. Chem. Front.* **2019**, *6*, 2365–2368.
- (52) Guo, S.-P.; Chi, W.; Zou, J.-P.; Xue, H.-G. Crystal and Electronic Structures, and Photoluminescence and Photocatalytic Properties of α-EuZrS₃. New J. Chem. **2016**, 40, 10219–10226.
- (53) Assoud, A.; Kleinke, H. Unique Barium Selenostannate—Selenide: $Ba_7Sn_3Se_{13}$ (and Its Variants $Ba_7Sn_3Se_{13-\delta}Te_{\delta}$) with $SnSe_4$ Tetrahedra and Isolated Se Anions. *Chem. Mater.* **2005**, *17*, 4509–4513.
- (54) Yuan, F.-Y.; Lin, C.-S.; Huang, Y.-Z.; Zhang, H.; Zhou, A.-Y.; Chai, G.-L.; Cheng, W.-D. BaCdGeSe₄: Synthesis, Structure and Nonlinear Optical Properties. *J. Solid State Chem.* **2021**, 302, No. 122352.
- (55) Dou, Y.; Chen, Y.; Li, Z.; Iyer, A. K.; Kang, B.; Yin, W.; Yao, J.; Mar, A. SrCdGeS₄ and SrCdGeSe₄: Promising Infrared Nonlinear Optical Materials with Congruent-Melting Behavior. *Cryst. Growth Des.* **2019**, *19*, 1206–1214.
- (56) Zhen, N.; Wu, K.; Wang, Y.; Li, Q.; Gao, W.; Hou, D.; Yang, Z.; Jiang, H.; Dong, Y.; Pan, S. BaCdSnS₄ and Ba₃CdSn₂S₈: Syntheses, Structures, and Non-Linear Optical and Photoluminescence Properties. *Dalton Trans.* **2016**, *45* (26), 10681–10688.
- (57) Jana, S.; O'Donnell, S.; Leahy, I. A.; Koldemir, A.; Pöttgen, R.; Smaha, R. W.; Maggard, P. A. Synthesis, Crystal Structure, and Physical Properties of the Eu(II)-Based Selenide Semiconductor: EuHfSe₃. *J. Mater. Chem. C* **2024**, *12*, 11769–11777.
- (58) Bera, T. K.; Kanatzidis, M. G. $Na_2EuAs_2S_5$, $NaEuAsS_4$, and $Na_4Eu(AsS_4)_2$: Controlling the Valency of Arsenic in Polysulfide Fluxes. *Inorg. Chem.* **2012**, *51*, 4293–4299.
- (59) Mar, A.; Ibers, J. A. Structure of Europium Zirconium Selenide, EuZrSe₃. *Acta Cryst. C* **1992**, *48*, 771–773.
- (60) Łątka, K. Magnetism and Hyperfine Interactions in GdT_2Si_2 Systems, Report No1443/PS; Institute of Nuclear Physics: Cracow; 1989; Chapter 5, p 68.
- (61) Czjzek, G.; Oestreich, V.; Schmidt, H.; Łątka, K.; Tomala, K. A Study of Compounds GdT₂Si₂ by Mössbauer Spectroscopy and by Bulk Magnetization Measurements. *J. Magn. Magn. Mater.* **1989**, *79*, 42–56.
- (62) Pöttgen, R.; Johrendt, D. Equiatomic Intermetallic Europium Compounds: Syntheses, Crystal Chemistry, Chemical Bonding, and Physical Properties. *Chem. Mater.* **2000**, *12*, 875–897.
- (63) Abudurusuli, A.; Wu, K.; Pan, S. Four New Quaternary Chalcogenides A₂Ba₇Sn₄Q₁₆ (A = Li, Na; Q = S, Se): Syntheses, Crystal Structures Determination, Nonlinear Optical Performances Investigation. *New J. Chem.* **2018**, *42*, 3350–3355.
- (64) Duan, R.; Lin, H.; Wang, Y.; Zhou, Y.; Wu, L. Non-Centrosymmetric Sufides $A_2Ba_6MnSn_4S_{16}$ (A = Li, Ag): Syntheses, Structures and Properties. *Dalton Trans.* **2020**, *49*, 5914–5920.
- (65) Feng, P.; Zhang, J.-X.; Ran, M.-Y.; Wu, X.-T.; Lin, H.; Zhu, Q.-L. Rare-earth-based chalcogenides and their derivatives: an encouraging IR nonlinear optical material candidate. *Chem. Sci.* **2024**, *15*, 5869–5896.
- (66) Yu, P.; Zhou, L.-J.; Chen, L. Noncentrosymmetric Inorganic Open-Framework Chalcohalides with Strong Middle IR SHG and

Red Emission: $Ba_3AGa_5Se_{10}Cl_2$ (A = Cs, Rb, K). *J. Am. Chem. Soc.* **2012**, 134, 2227–2235.

- (67) Li, Y.-Y.; Liu, P.-F.; Hu, L.; Chen, L.; Lin, H.; Zhou, L.-J.; Wu, L.-M. Strong IR NLO Material Ba₄MGa₄Se₁₀Cl₂: Highly Improved Laser Damage Threshold via Dual Ion Substitution Synergy. *Adv. Opt. Mater.* **2015**, *3*, 957–966.
- (68) Chung, I.; Malliakas, C. D.; Jang, J. I.; Canlas, C. G.; Weliky, D. P.; Kanatzidis, M. G. Helical Polymer $1/\infty[P_2Se_6^{2-}]$: Strong Second Harmonic Generation Response and Phase-Change Properties of Its K and Rb Salts. *J. Am. Chem. Soc.* **2007**, *129*, 14996–15006.
- (69) Lu, B.; Sayyad, S.; Sanchez-Martinez, M. A.; Manna, K.; Felser, C.; Grushin, A. G.; Torchinsky, D. H. Second Harmonic Generation in the Topological Multifold Semimetal RhSi. *Phys. Rev. Res.* **2022**, *4*, No. L022022.